

Fatigue Properties of Heat-Treated 30MSV6 Vanadium Microalloyed Steel

M. Hajisafari, S. Nategh, H. Yoozbashizadeh, and A. Ekrami

(Submitted August 18, 2011; in revised form March 18, 2012; published online August 23, 2012)

In the present study, 30MSV6 microalloyed steel was heat treated under different conditions, and the relation between its microstructure and mechanical properties was investigated. Scanning electron microscopy and transmission electron microscopy were used to characterize the microstructure of the heat-treated steel, and the effect of microstructure on tensile strength and fatigue behavior was determined. Microstructural analysis indicated that precipitates were formed at different sites such as grain boundaries and sub-grain boundaries. Furthermore, microstructural studies accompanied by the evaluation of mechanical properties revealed that the optimal heat treatment cycle of 30MSV6 microalloyed steel involved austenitization at 1223 K for 1 h and cooling in air to room temperature, followed by aging at 873 K for 1.5 h. The optimal heat treatment cycle resulted in significant improvement in the fatigue strength, tensile strength, and ductility because of the development of a uniform distribution of fine precipitates in a refined microstructure. The fatigue limit under optimum conditions (~ 384 MPa) was greater than that under other conditions (~ 321 and 312 MPa).

Keywords fatigue, heat treatment, microalloyed steel, microstructure

1. Introduction

The mechanical properties of the microalloyed steels are favorable to both manufacturing and service performance of automotive components. Depending on deformation temperature, cooling rate, and the composition, a variety of microstructures in microalloyed steels can be obtained (Ref 1, 2). Microalloyed steels can be heat treated to obtain dual phase and multiphase microstructures. There have been detailed investigations on microstructural evolutions during different heat treatments and their influence on tensile behavior of microalloyed steels (Ref 3). The strength, ductility, and fatigue resistance of microalloyed steels can be attributed to their microstructural aspects (Ref 4, 5).

Bhat and Fine (Ref 6) indicated that the initial formation of a fatigue crack as a nucleation process was due to random fluctuations of a metastable assembly of defect structures generated during cycling for a pure iron and a high-strength low-alloy steel produced by hot rolling. Over the last two decades, research has been focused on the thermomechanical processing to enhance strength, toughness, and fatigue strength of

microalloyed steels. Numerous investigations have been conducted to determine the effect of microstructural evolution on fatigue behavior of microalloyed steels. These studies have usually separately characterized the effect of heat treatment on precipitates, microstructure, and mechanical properties (Ref 3-7).

Although the effect of heat treatment on fatigue behavior has been clarified, the influence of optimum cooling rate and aging temperature on 30MSV6 microalloyed steel has not been investigated extensively or in detail. It has been shown only for several microalloyed steels that fatigue behavior is quite different for microstructures produced under different forging and hot-rolling conditions. For example, Sankaran et al. (Ref 5) investigated the monotonic, cyclic stress-strain, and low cycle fatigue behavior of 38MnSiVS5 microalloyed steel having different microstructures resulting from different forging conditions. Fatigue crack initiation and propagation mechanisms corresponding to different microstructural conditions have also been compared. Also, Sankaran et al. (Ref 7) investigated the high cycle fatigue (HCF) behavior of 38MnSiVS5 microalloyed steel which had experienced controlled thermomechanical processing to generate a multiphase microstructure. The fatigue limit, fatigue thresholds, crack growth, and crack closure characteristics were identified. Furthermore, Laurito et al. (Ref 3) evaluated the effects of microstructure on fatigue crack growth behavior of the low carbon-manganese microalloyed steel. They demonstrated that the distinct microstructural conditions were obtained by means of inter-critical and isothermal heat treatments followed by water quench, in which the material specimens were kept at different temperatures of 1073, 1223, and 1473 K. Therefore, in the present study, a new approach for optimizing the fatigue behavior of the 30MSV6 vanadium microalloyed steel through precipitation hardening under various aging and cooling conditions was studied. The effects of these conditions on microstructure as well as mechanical properties such as ductility, and yield and tensile strengths were characterized. Then, the optimum treatment

M. Hajisafari and S. Nategh, Department of Materials Engineering, Science and Research Branch, Islamic Azad University, Tehran, Iran; and H. Yoozbashizadeh and A. Ekrami, Department of Materials Science and Engineering, Sharif University of Technology, Tehran, Iran. Contact e-mail: hajisafari@iauyazd.ac.ir.

regarding a preferred combination of ductility and yield strength was determined. Finally, fatigue behavior (i.e., crack initiation and S-N curve behaviors) undergone by the specimen under the optimum condition of treatment was studied. Furthermore, transmission electron microscopy (TEM) studies on microstructure and morphology of precipitates were conducted to illustrate the variation of mechanical properties with heat-treatment conditions.

1.1 Experimental Procedures

High-strength microalloyed steel produced by the Iran Alloy Steel Company, in the form of hot-rolled and air-cooled rods, 20 mm in diameter with the composition shown in Table 1, were used in our investigation.

The AC3 temperature was calculated according to Andrews equation (Ref 8), and austenitizing temperatures were selected to be in the range of 1173-1253 K. Austenitization was for 1 h in an electric furnace operating under argon atmosphere. Three different cooling mediums, such as cooling in air (AC), cooling in insulated stainless steel cylinder (ISSC), and cooling by fan (FC) were used for cooling. A data logger that records the time and temperature during cooling was used to measure the cooling rate. The cooling rates for FC, AC, and ISSC were; 6.4, 3.8, and 0.9 K/s, respectively. In order to determine the effect of aging temperature on precipitation and strengthening, the aging treatment was done at temperature range of 843-913 K for 1.5 h (Fig. 1).

Tensile specimens were CNC-machined according to ASTM-E8M standard (Ref 9). Specimens were then polished into fine surfaces, and then our in-house Universal Testing Machine GOTECH GT-7001-LC30 was used with a constant crosshead speed of 0.05 mm/min for tensile testing. The fatigue specimens were prepared according to ASTM-E466 standard (Ref 10). After machining, emery papers of 320-3000 grit were used to polish the surface of specimens. To achieve a fine

surface finish, specimens were finally polished by cotton. The fatigue test was done using SANTAM rotating-bending fatigue testing machine (SANTAM, Ltd. IRAN) at different stress amplitudes at $R = -1$. Stress Amplitudes were selected in the range of 280-640 MPa.

Optical microscope and scanning electron microscope (SEM, LEO 440i) were used for microstructural characterization. For etching of specimens, 2% Nital etchant was selected. A digital image processor program was used to determine the pro-eutectoid ferrite size and pearlite interlamellar spacing. TEM (200 kV, JEOL 2010) was accomplished on specimens prepared by ion milling to study precipitates. In addition, energy dispersive spectroscopy (EDS) and selected area diffraction pattern (SADP) were used, respectively, for the analysis and indication of the crystal structure of the precipitates.

2. Results and Discussion

2.1 Microstructures

In Fig. 2 and 3, the effects of different cooling rates on the microstructure are seen, respectively, in optical and SEM micrographs of heat-treated specimens. It is seen in Fig. 2(a) that the as-received specimen represents pearlite and polygonal pro-eutectoid ferrite. Furthermore, microstructural studies revealed that increasing the cooling rate from austenitizing temperature results in the reduction of pro-eutectoid ferrite size. Similarly, Laurito et al. (Ref 3) and Jahazi and Eghbali (Ref 11) reported the effect of cooling rate on the ferrite size in a low-carbon microalloyed steel and two microalloyed forging steels. As seen in Fig. 2, with an increase in cooling rate, the equiaxed morphology of the pro-eutectoid ferrites in the as-received specimen (Fig. 2a) has been converted to a lath-type one (Fig. 2b-d). This phenomenon is generally associated with the influence of cooling rate on the growth rates of ferrite (Ref 11). A high cooling rate suppresses the $\gamma \rightarrow \alpha$ transformation and increases the nucleation rate of pro-eutectoid ferrite. Therefore, 6.4 K/s cooling rate for the specimens would be expected to give a finer microstructure compared with specimens cooled with 3.8 and 0.9 K/s cooling rates. It is clear that the $\gamma \rightarrow \alpha$ transformation occurs in two steps: nucleation, and then growth. During nucleation, a new interface is generated that separates the product pro-eutectoid ferrite phase from the parent austenite phase. This interface migrates into the surrounding parent phase during the subsequent growth. Cooling rate from

Table 1 Chemical composition (wt.%) of the 30MSV6 microalloyed steel

Elements	C	Si	Mn	P	S	Cr
wt.%	0.3	0.54	1.47	0.0167	0.05	0.21
Elements	Mo	Ni	Al	V	Ti	N
wt.%	0.005	0.1	0.022	0.11	0.017	≥120 ppm

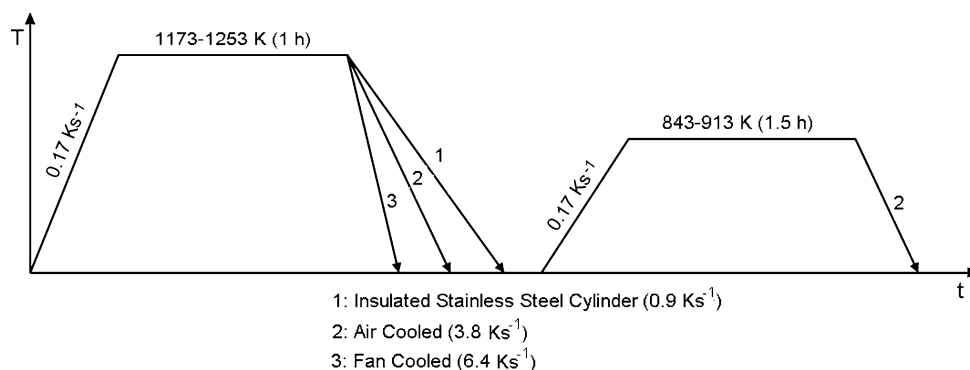


Fig. 1 Schematic diagram showing heat-treatment process of specimens investigated

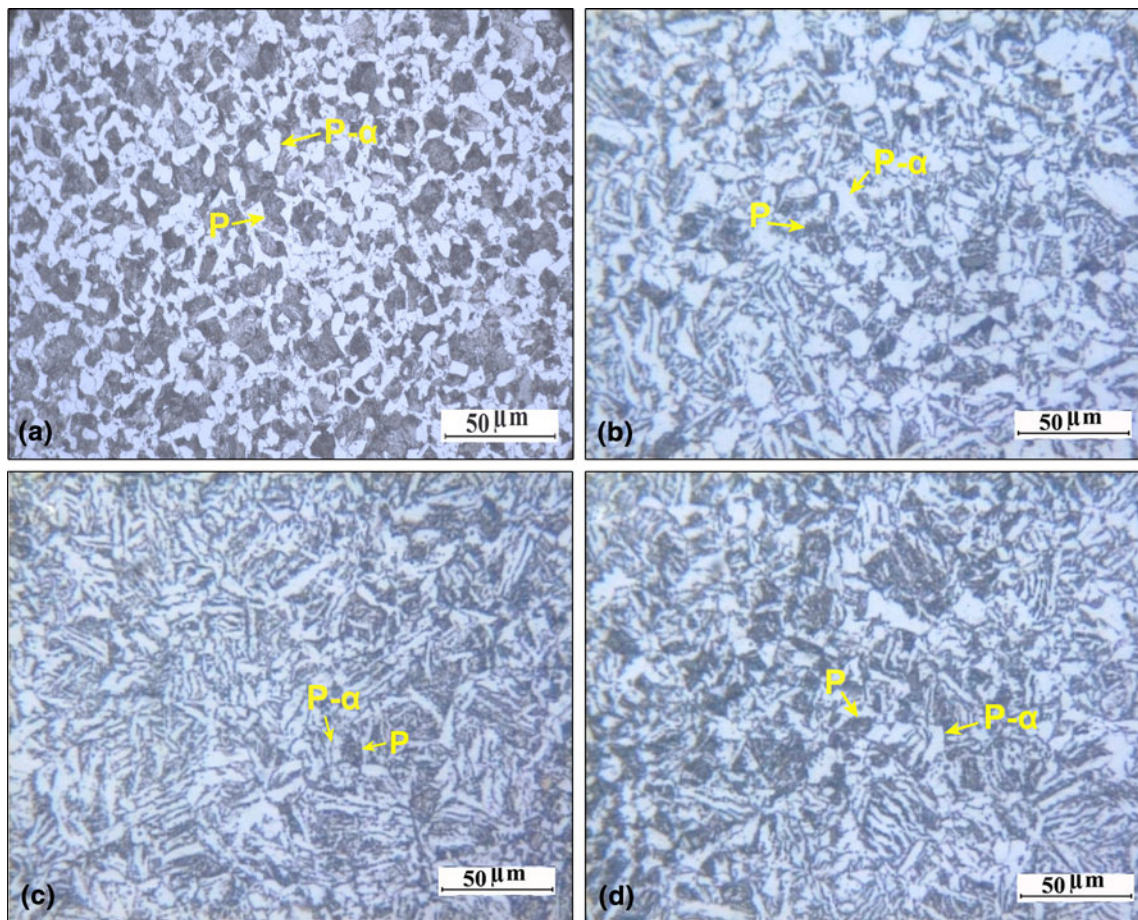


Fig. 2 Optical micrographs for specimens which experienced different cooling conditions; they were all austenitized at 1223 K for 1 h and aged at 873 K for 1.5 h: (a) As-received; (b) 0.9 K/s; (c) 3.8 K/s; and (d) 6.4 K/s; P is pearlite and P- α is pre-eutectoid ferrite

austenitizing temperature affects the nucleation and growth phenomena. Gunduz and Capar (Ref 12) showed similar results for the microstructure and properties of forged medium carbon microalloyed steels, which had experienced cooling in different media such as air, sand, and water.

As seen in Fig. 3 and Table 2, the increasing cooling rate reduces the pearlite interlamellar spacing. This result can be related to the influence of cooling rate on transformation temperature. As the cooling rate is increased, the under cooling is decreased. Therefore, the driving force for transformation is increased which results in finer pearlite interlamellar spacing. To be more precise, the increasing cooling rate caused variation of diffusion kinetics. In general, the slow diffusivity at low temperatures reduces the diffusion distance and consequently reduces the pearlite interlamellar spacing. Also, According to previous investigations, interlamellar spacing is dependent on the transformation temperature and is inversely proportional to under-cooling below the eutectoid temperature (Ref 13). The relationship between interlamellar spacing and transformation conditions is in accordance with the change in the growth rate. The exact variations of matrix constituents versus heat-treatment conditions as well as the matrix constituents of the as-received specimen, together with their mechanical properties, are presented in Table 2. As seen in this table, austenitization temperatures did not influence the microstructure and micro-constituents of matrix. The steel contains 0.017 wt.% Ti

that inhibits the growth of the initial austenite grains during the process.

In order to study the effect of microstructure on the mechanical properties, TEM studies were carried out on the austenitized specimen at 1223 K for 1 h, 3.8 K/s cooling rate, and aging at 873 K for 1.5 h. According to the TEM observations, three different precipitations such as random precipitation, interphase precipitation, and heterogeneous precipitation on the dislocations were identified (Fig. 4, 5). Figure 4(a) shows a bright-field TEM micrograph of precipitates formed within pre-eutectoid ferrites and phase boundaries. Figure 4(b) and (c) shows SADP and the EDX analyses of the precipitate indicated by P-arrow in Fig. 4(a). The EDX and SADP of the precipitate revealed that this precipitate was (V,Ti)C. According to this SADP, the crystal structure of this precipitate is a face center cubic unit cell of NaCl type, and the lattice parameter of this precipitate was calculated to be about 4.34 Å. This calculated lattice parameter is very close to the reported value for the vanadium-titanium carbide ((V,Ti)C) (Ref 18). Figure 4(d) and (e) shows the SADP and the EDX analyses of the matrix indicated by M-arrow in Fig. 4(a). The lattice parameter of the matrix was calculated to be about 2.53 Å. The EDX and SADP of the matrix revealed that this phase is ferrite (α). The orientation relationship between ferrite and (V,Ti)C is a cube-cube $[111]_{\alpha}/[001]_{(V,Ti)C}$ one, and $\alpha/(V,Ti)C$ interface is not coherent.

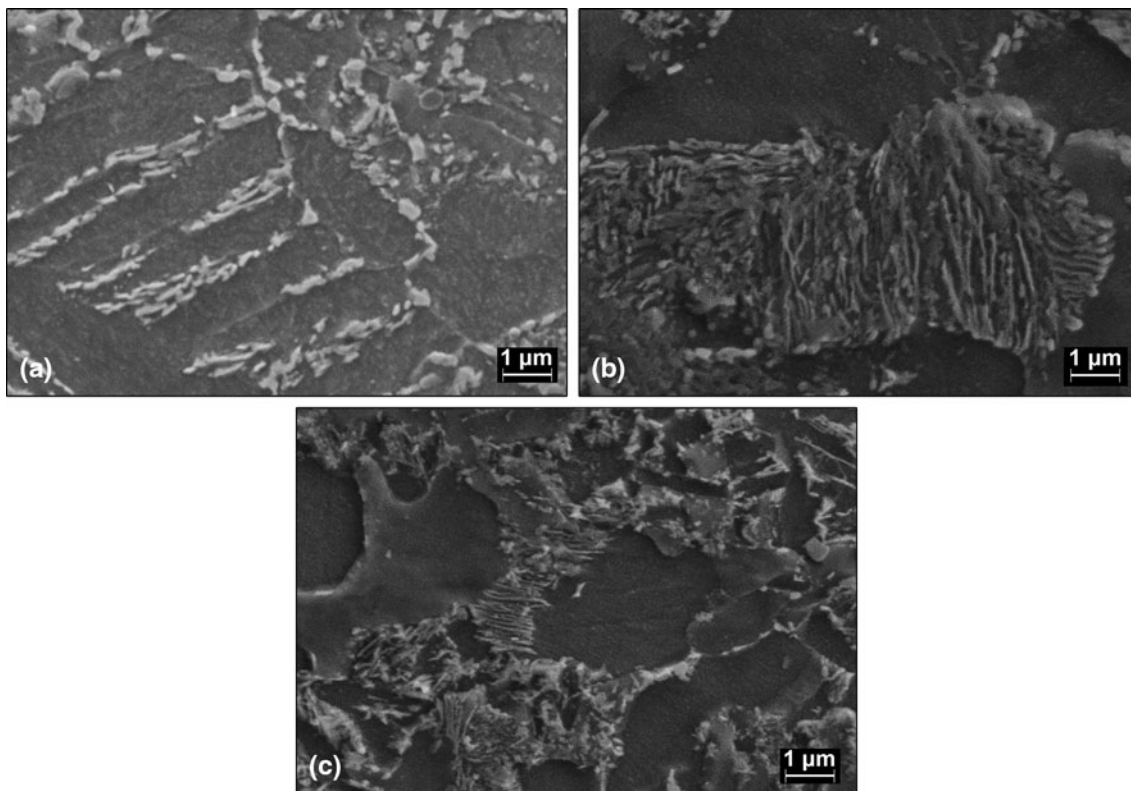


Fig. 3 SEM micrographs of specimens austenitized at 1223 K for 1 h, cooled at different rates, and aged at 873 K for 1.5 h: (a) 0.9 K/s; (b) 3.8 K/s; and (c) 6.4 K/s

Figure 5(a) shows a bright-field TEM micrograph of parallel sheets consisting of fine precipitates formed repeatedly with regular spacing placed on dislocations. The formation of precipitates on the dislocations can be explained by the reduction of strain-field energy between the precipitates and matrix (Ref 14-17). Figure 5(b) and (c) shows the SADP and EDS analyses of the precipitates indicated by P-arrow in Fig. 5(a). Figure 5(d) and (e) shows the SADP and EDS analyses of the matrix around the precipitates indicated by M-arrow in Fig. 5(a). The different parts of Fig. 5 revealed that (I) The precipitates in this specimen are mainly VC. (II) The calculated lattice parameter of VC is 4.26 Å. Furthermore, crystal structure of this carbide is a face centered cubic unit cell of NaCl type, which is in good agreement with previous reported ones (Ref 18). (III) The calculated lattice parameter and crystal structure of the matrix is 2.53 Å and body centered cubic, which indicates that the matrix is ferrite. (IV) The orientation relationship between pro-eutectoid ferrite and VC is a cube-cube one ($[111]_{\alpha}/[001]_{VC}$), and α/VC interface is non-coherent.

2.2 Mechanical Properties

Tensile properties of the specimens, including yield and tensile strengths as well as elongation, were determined for the various cooling rates and aging temperatures, as presented in Table 2. As seen in this table, initially, the yield and tensile strengths increase by increasing the cooling rate but afterward, these properties decrease. Important factor affecting the strength of these specimens is the pro-eutectoid ferrite size that was produced after cooling from the austenitizing

temperature. Finer pro-eutectoid ferrite size can be produced by lower $\gamma \rightarrow \alpha$ transformation temperatures, which results in greater strength and improved ductility. A decrease in the transformation temperature, which is due to an increase in cooling rate, affects the level of precipitation strengthening. These precipitates are closely spaced and obstruct mobile dislocations, resulting in higher strengths. Furthermore, pearlite interlamellar spacing has a positive effect on the mechanical properties of specimens, as reported in other studies (Ref 11). In addition, the ductility improvement is a result of refinement of pro-eutectoid ferrite. It also has been shown that the yield and tensile strengths as well as ductility were quite different for AC (3.8 K/s), ISSC (0.9 K/s), and FC (6.4 K/s) specimens because of the difference in precipitate size, pro-eutectoid ferrite size, and pearlite interlamellar spacing.

Fatigue behaviors of heat-treated specimens austenitized at 1223 K, followed by different cooling rate, and aged at 873 K for 1.5 h are presented in Fig. 6. Fatigue limit was defined, for the specimen with 3.8 K/s cooling rate, as the stress amplitude at which failure did not occur up to 1.7×10^6 cycles. It was determined to be 384 MPa that was greater than the fatigue limit of specimens with cooling rates of 6.4 K/s (321 MPa) and 0.9 K/s (312 MPa). Therefore, a good combination of fatigue and tensile properties was obtained in the heat-treated specimen with the following conditions: austenitizing at 1223 K for 1 h, 3.8 K/s cooling rate, and aging at 873 K for 1.5 h. This heat-treatment cycle was selected as the optimal condition for the 30MSV6 microalloyed steel. It is worth noting that, the optimal heat treatment condition resulted in an improvement in the ultimate tensile strength, yield strength, and ductility of 30MSV6 microalloyed steel about 4.3, 15.8, and 26.6%,

Table 2 Microstructure specification and mechanical properties at different austenitization and aging temperatures (austenitization period: 1 h and aging period: 1.5 h)

Characteristics	Pearlite interlamellar spacing, μm	Pre-eutectoid ferrite size, μm	Pre-eutectoid ferrite aspect ratio, %	YS, MPa	UTS, MPa	E , %	σ_Y/σ_{UTS}	
As-received	0.268 ± 0.05	2.54 ± 0.5	27.58	648.9	807.8	14.3	0.803	
Austenitizing temperature, $^{\circ}\text{C}$	Ageing temperature, $^{\circ}\text{C}$	Pearlite interlamellar spacing, μm	Pre-eutectoid ferrite size, μm	Pre-eutectoid ferrite aspect ratio, %	YS, MPa	UTS, MPa	E , %	σ_Y/σ_{UTS}
Cooling medium: ISSC								
1173	843	0.217 ± 0.04	2.19 ± 0.4	16.29	664.6	809.4	18.1	0.821
	873	0.218 ± 0.07	2.21 ± 0.4	17.8	671.4	804.8	17.9	0.834
	913	0.210 ± 0.04	2.25 ± 0.5	16.02	667.3	801.9	17.4	0.832
1223	843	0.221 ± 0.05	2.39 ± 0.3	16.9	646.5	779.2	16.25	0.835
	873	0.208 ± 0.06	2.28 ± 0.4	17.12	653.2	768.4	19.5	0.85
	913	0.213 ± 0.04	2.36 ± 0.3	15.93	652.4	750.8	17.5	0.869
1253	843	0.219 ± 0.08	2.42 ± 0.2	16.23	628.4	721.6	17.3	0.871
	873	0.232 ± 0.07	2.45 ± 0.3	15.32	632.8	732.1	16.82	0.864
	913	0.209 ± 0.06	2.45 ± 0.2	15.84	610.3	709.7	16.9	0.86
Cooling medium AC								
1173	843	0.128 ± 0.03	1.79 ± 0.5	21.12	704.2	821.8	16.8	0.857
	873	0.126 ± 0.05	1.74 ± 0.4	20.15	710	825.4	16.6	0.831
	913	0.124 ± 0.05	1.84 ± 0.3	21.21	694.4	819.8	17.3	0.847
1223	843	0.145 ± 0.04	1.92 ± 0.5	20.29	680.3	772.9	18.7	0.88
	873	0.127 ± 0.05	1.96 ± 0.4	19.89	750.9	843.1	18.1	0.891
	913	0.141 ± 0.04	1.95 ± 0.3	20.04	639.1	781.6	19.2	0.818
1253	843	0.130 ± 0.07	1.99 ± 0.1	19.78	653.2	765.2	18.8	0.854
	873	0.139 ± 0.06	2.07 ± 0.2	19.88	661.2	778.2	18.9	850
	913	0.127 ± 0.04	2.10 ± 0.2	20.14	643.7	770.6	17.8	0.835
Cooling medium: FC								
1173	843	0.100 ± 0.03	1.21 ± 0.4	25.94	684.5	815.2	15.9	0.84
	873	0.090 ± 0.04	1.12 ± 0.3	25.42	697	827.8	15.7	0.843
	913	0.101 ± 0.05	1.17 ± 0.4	26.32	663.3	800.2	15.3	0.829
1223	843	0.102 ± 0.04	1.23 ± 0.5	24.91	678.5	800.4	16.1	0.848
	873	0.089 ± 0.04	1.26 ± 0.3	26.55	641.5	812.2	16	0.79
	913	0.091 ± 0.05	1.25 ± 0.4	24.29	635.2	788.2	15.4	0.806
1253	843	0.103 ± 0.03	1.40 ± 0.3	25.74	671.4	749.1	15.8	0.896
	873	0.099 ± 0.04	1.48 ± 0.3	25.83	684.2	793.4	115.3	0.862
	913	0.110 ± 0.01	1.43 ± 0.5	24.12	664.7	765.3	15.4	0.869

respectively, in comparison with the as-received specimen. Also, the fatigue limit of the specimen that had experienced optimum conditions of heat treatment was better than those specimens cooled at 6.4 and 0.9 K/s cooling rates. This improvement in fatigue strength can be related to the ratio of yield strength to ultimate tensile strength (σ_Y/σ_{UTS}). On the other hand, it has been found that higher ratio of σ_Y/σ_{UTS} resulted in greater fatigue limit (Table 2). Furthermore, the improvement in the fatigue and tensile properties of optimal heat-treated specimen can be related to the refinement in the pro-eutectoid ferrite size, interlamellar spacing of pearlite, and the formation of precipitates at different sites of matrix as mentioned in section 3.1, i.e., optimal heat treatment reduces the size of pre-eutectoid ferrite and interlamellar spacing of pearlite. Furthermore, during optimal heat treatment, fine (V,Ti)C and VC precipitates are formed in the different sites of microstructure.

2.3 Fractography

Figure 7 shows the fractographs of the fatigue specimen that had been heat treated in optimal conditions. As shown in this

figure, initiation of cracking happened in the surface of specimen (Fig. 7a). As shown in Fig. 7(b), propagation of fatigue crack in this specimen was predominant in the pro-eutectoid ferrite-pearlite microstructure through the ductile fracture mechanism of microvoid coalescence and growth. The voids appeared to nucleate at precipitates where the continuity between the matrix and the second phase particles was relatively weak. Striation-like features can also be observed in this specimen (Fig. 7c). The composite microstructure, mixture of ferrite and pearlite phases, caused the discontinuous striation features in the ferrite-pearlite steel. On the other hand, the least resistance path to fatigue crack growth was through the ferrite and the stronger pearlite colonies tended to retard the crack growth (Ref 5).

All specimens show some internal cracks at MnS inclusion interface. Figure 8 shows the morphology and analysis of one these inclusions. Figure 8(a) indicates an example of MnS inclusions, which acts as the origin of an initiation crack. Figure 8(b) shows an EDS of the inclusion in Fig. 8(a). According to Fig. 8(a), internal cracks may form in HCF regime. However, earlier experimental studies by Japanese

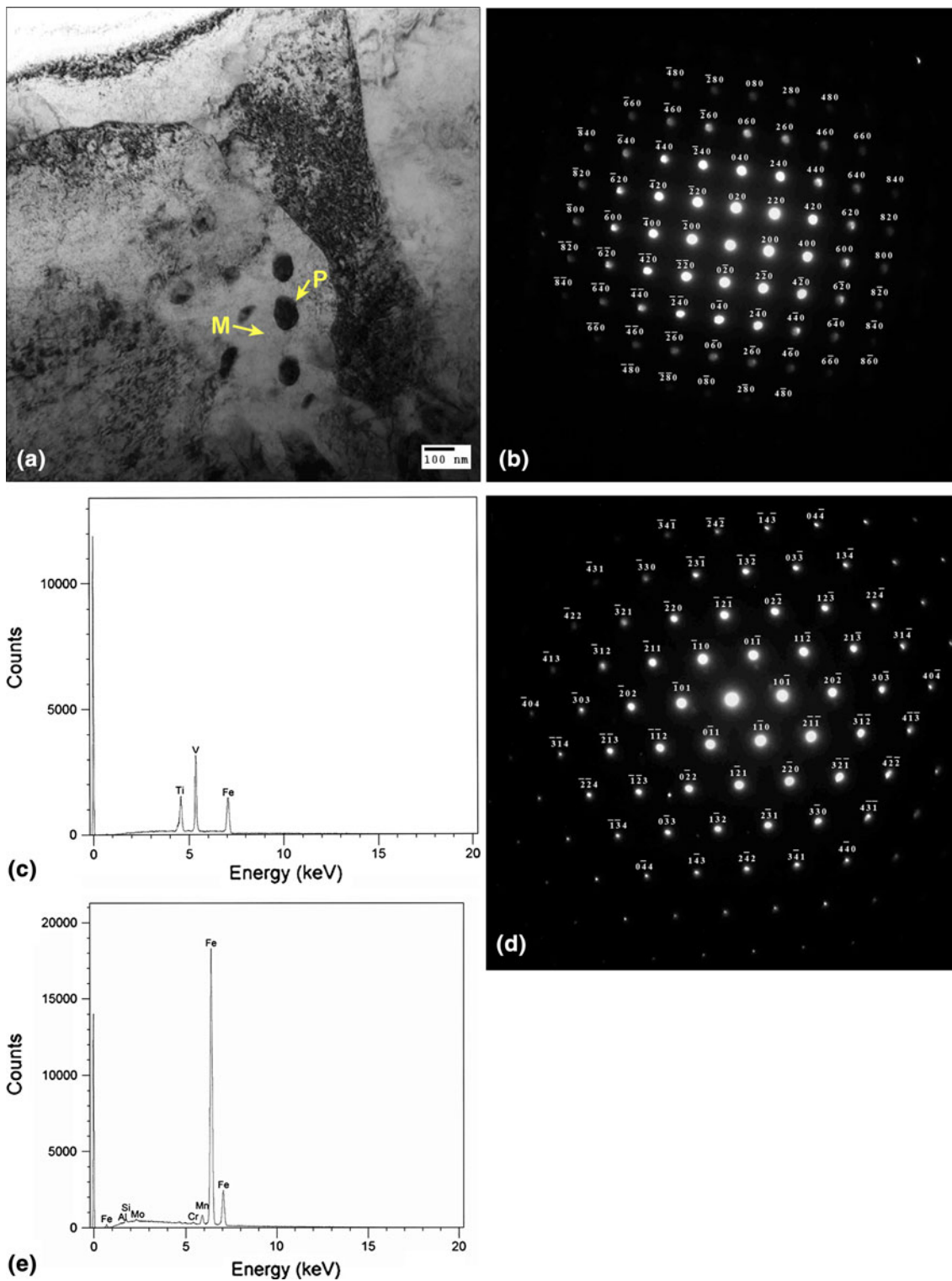


Fig. 4 (a) Bright-field TEM micrographs of fine precipitates distributed randomly in pre-eutectoid ferrite phase and at grain boundaries; (b) SADP for the precipitate shown in image a (P-arrow); (c) EDS analysis of the precipitate shown in image a (P-arrow); (d) SAD pattern for the matrix around the precipitate shown in image a (M-arrow); and (e) EDS analysis of the matrix around the precipitate shown in image a (M-arrow)

researchers (Ref 19, 20) show slightly different results. They indicated a change of crack initiation location from the surface of the specimens in the HCF regime to a subsurface crack initiation at inclusions in the very high cycle fatigue (VHCF)

regime for low-alloy steels. Particularly, in rotating-bending experiments, the S-N curve shows a plateau-like regime in the range of 10^6 cycles, at stress amplitudes, where surface crack initiation leads to HCF failure and slightly lower stress

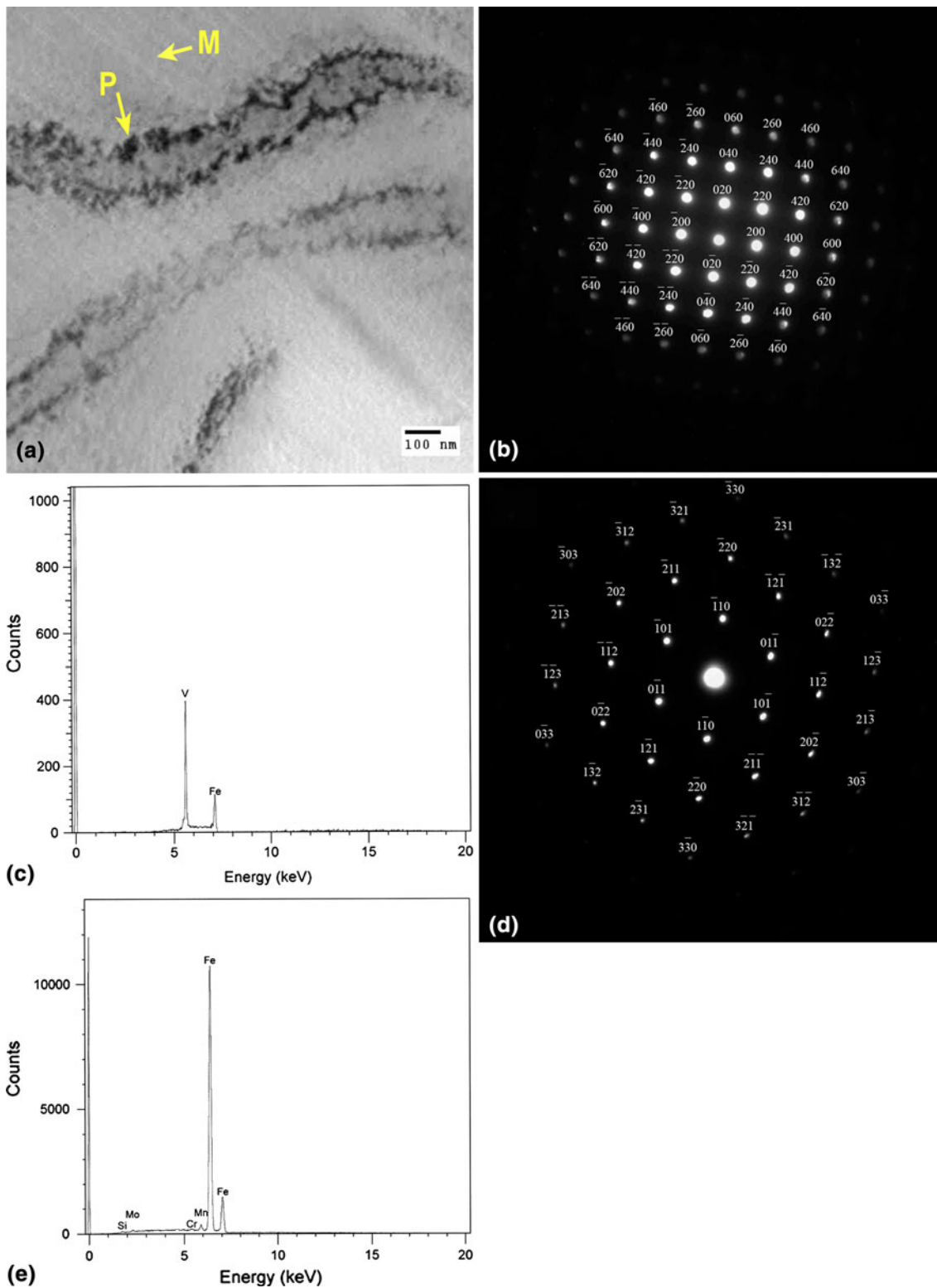


Fig. 5 (a) Bright-field TEM micrographs of fine precipitates heterogeneously nucleated on dislocations; (b) SAD pattern for the precipitate shown in image a (P-arrow); (c) EDS analysis of the precipitate shown in image a (P-arrow); (d) SAD pattern for the matrix around the precipitate shown in image a (M-arrow); and (e) EDS analysis of the matrix around the precipitate shown in image a (M-arrow)

amplitudes cause crack initiation at internal inclusions and VHCF failure.

The fatigue crack propagation paths for all conditions are shown in Fig. 9. It can be observed that the fatigue crack in the

heat-treated specimen creating a tendency to deviate from the pearlite and to propagate mainly through the pro-eutectoid ferrite, resulting in a more tortuous crack path. Under optimum heat treatment conditions, the internal fatigue cracks had a

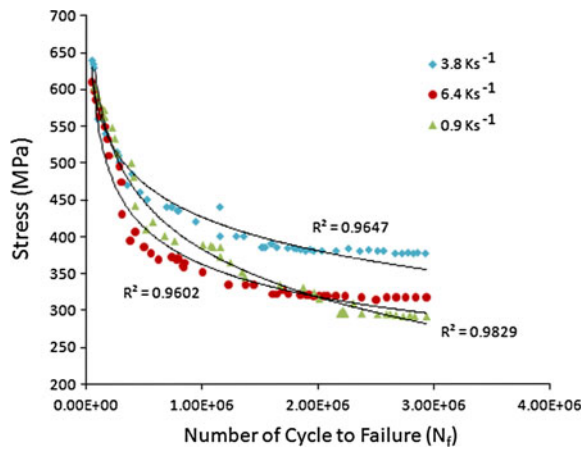


Fig. 6 S-N curves of 30MSV6 vanadium microalloyed steel considering all the conditions in the present study

lower density than other specimens (Fig. 9b), because of a refinement of pre-eutectoid ferrite phase in this specimen.

3. Conclusion

Based on the results achieved and to have an excellent yield and ultimate tensile strengths and good ductility together with increased fatigue strength for the 30MSV6 microalloyed steel, the optimal cooling rate, austenitizing, and aging temperatures can be reported as 3.8 K/s, 1223 K for 1 h, and 873 K for 1.5 h, respectively. This combination of optimum properties is related to the interlamellar spacing of pearlite, pro-eutectoid ferrite size, and the presence of (V,Ti)C and VC precipitates formed on grain and sub-grain boundaries or randomly distributed within the pro-eutectoid ferrite phase. SEM characterization of fracture surfaces indicates that ductile fracture

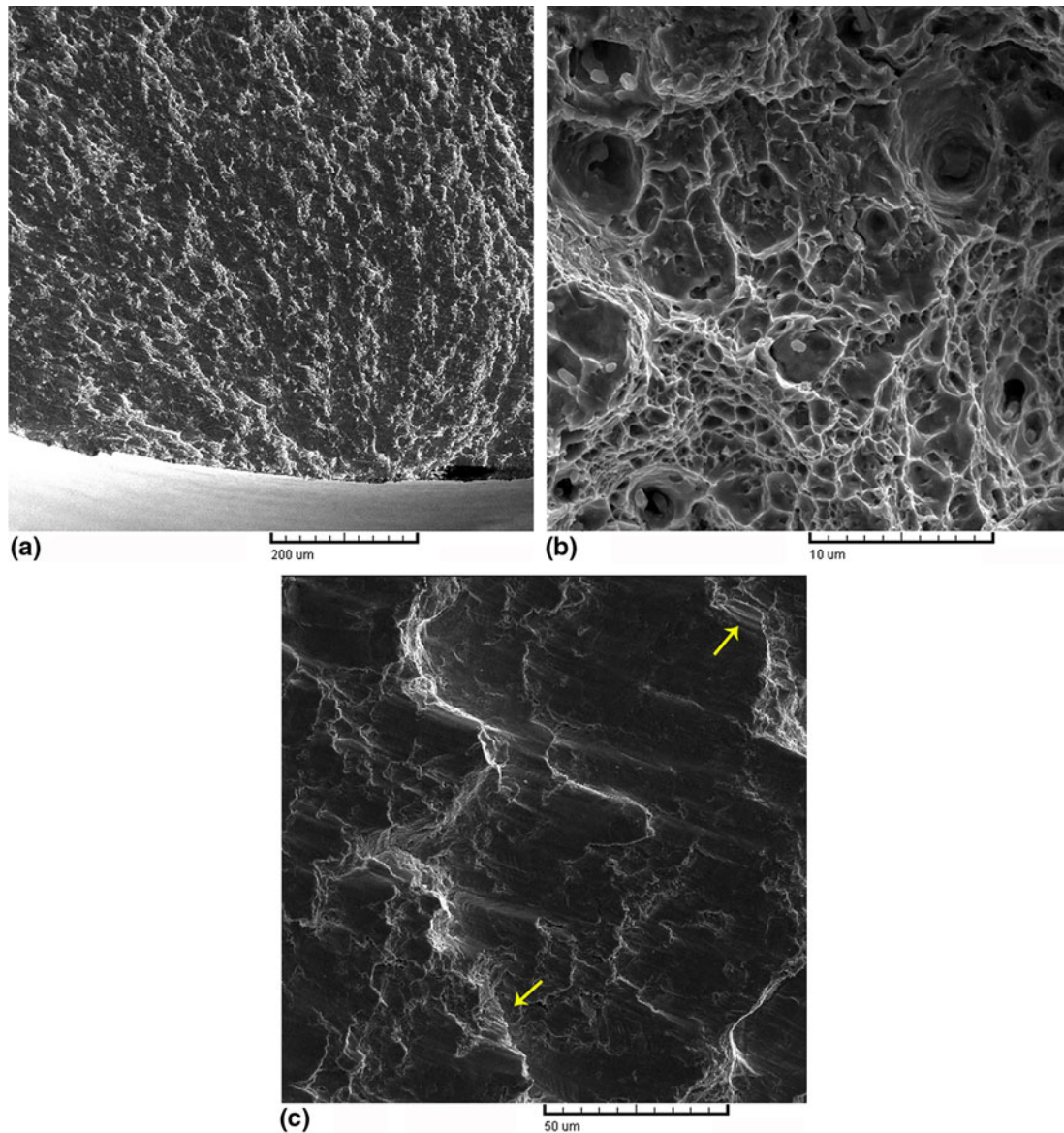


Fig. 7 SEM micrographs of room temperature fatigue fracture surface of the specimen austenitized at 1223 K for an hour, air cooled, and finally aged at 873 K for 1.5 h: (a) Crack initiation in the surface; (b) ductile fracture mechanism of microvoid coalescence and growth; and (c) striation-like features

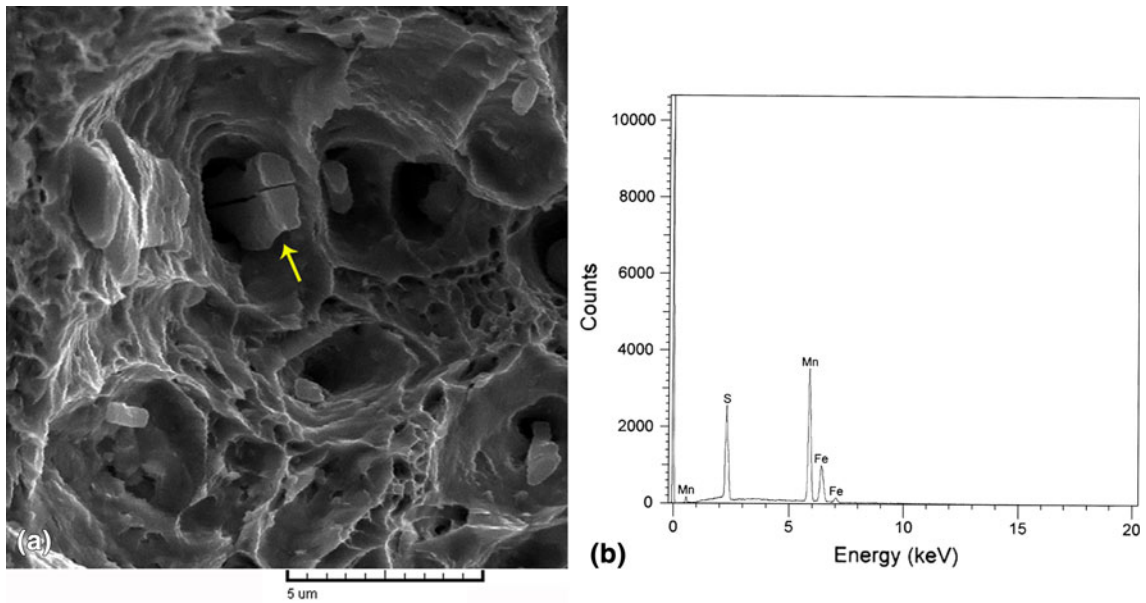


Fig. 8 SEM characterization of the fracture surface of the room temperature fatigue specimen: (a) MnS inclusion in a dimple; and (b) EDS of the MnS particle

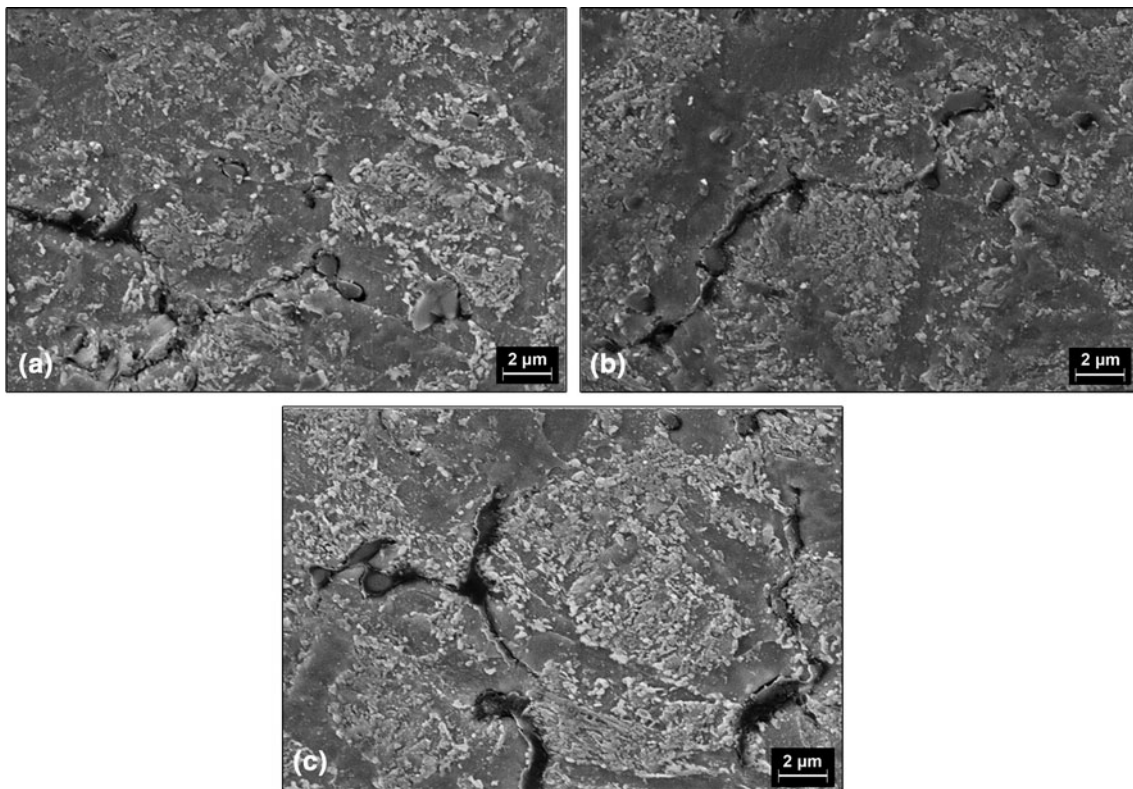


Fig. 9 SEM micrographs indicating fatigue crack propagation path in 30MSV6 microalloyed steel, cooled at different rates: (a) 0.9 K/s; (b) 3.8 K/s; and (c) 6.4 K/s

occurs and cracks initiate by micro-void formation and coalescence, which finally propagate and cause the fractures of the specimen. Furthermore, SEM studies revealed that some internal cracks may be formed at MnS inclusions in HCF

regime. The fatigue limit of the specimen that had experienced optimum conditions of heat treatment was 384 MPa which is about 16.6 and 18.7% higher than those of the specimens with cooling rates of 6.4 and 0.9 K/s. Comparing the mechanical

properties of the as-received material with those of optimal heat-treated specimen showed improvements by about 4.3, 15.8, and 26.3% for UTS, YS, and ductility, respectively.

Acknowledgments

The support provided by the Iran Alloy Steel Company is gratefully acknowledged. The help extended by the technical staff engineers, Mr. Kardi, Mr. Mosavi, Mr. Rezaie, and Mr. Meamari is appreciated. Also, the authors wish to thank the Science and Research Branch, Islamic Azad University. Finally, they specially offer their thanks to Mrs. Eshghi and the Materials characterization Ltd.

References

1. R. Steiner, *ASM Handbook. Properties and Selection: Irons, Steels, and High Performance Alloys*, ASM International, Materials Park, 1990
2. D.K. Matlock, G. Krauss, and J.G. Speer, Microstructure and Properties of Direct-Cooled Microalloy Forging Steels, *Mater. Process. Technol.*, 2001, **117**, p 324–328
3. D.F. Laurito, C.A.R.P. Baptista, M.A.S. Torres, and A.J. Abdalla, Microstructural Effects on Fatigue Crack Growth Behavior of a Microalloyed Steel, *Proc. Eng.*, 2010, **2**, p 1915–1925
4. U.P. Singh, A.M. Popli, D.K. Jain, B. Roy, and S. Jha, Influence of Microalloying on Mechanical and Metallurgical Properties of Wear Resistant Coach and Wagon Wheel Steel, *J. Mater. Eng. Perform.*, 2003, **12**, p 573–580
5. S. Sankaran, V. Subramanya Sarma, and K.A. Padmanabhan, Low Cycle Fatigue Behavior of a Multiphase Microalloyed Medium Carbon Steel: Comparison Between Ferrite-Pearlite and Quenched and Tempered Microstructures, *Mater. Sci. Eng. A*, 2003, **345**, p 328–335
6. S.P. Bhat and M.E. Fine, Fatigue Crack Nucleation in Iron and a High Strength Low Alloy Steel, *Mater. Sci. Eng. A*, 2001, **314**, p 90–96
7. S. Sankaran, V. Subramanya Sarma, K.A. Padmanabhan, G. Jaeger, and A. Koethe, High Cycle Fatigue Behavior of a Multiphase Microalloyed Medium Carbon Steel: A Comparison Between Ferrite-Pearlite and Tempered Martensite Microstructures, *Mater. Sci. Eng. A*, 2003, **362**, p 249–256
8. K.W. Andrews, Empirical Formulae for the Calculation of Some Transformation Temperatures, *JISI*, 1965, **203**, p 721–727
9. “Standard Test Methods for Tension Testing of Metallic Materials,” E 8M, *Annual Book of ASTM Standards*, 2000, Vol. 03.01, ASTM, West Conshohocken, p 77–98
10. “Standard Practice for Conducting Force Controlled Constant Amplitude Axial Fatigue Tests of Metallic Materials,” E 466, *Annual Book of ASTM Standards*, 2000, Vol. 03.01, ASTM, West Conshohocken, p 493–497
11. M. Jahazi and B. Eghbali, The Influence of Hot Forging Conditions on the Microstructure and Mechanical Properties of Two Microalloyed Steels, *J. Mater. Process. Technol.*, 2001, **113**, p 594–598
12. S. Gunduz and A. Capar, Influence of Forging and Cooling Rate on Microstructure and Properties of Medium Carbon Microalloy Forging Steel, *J. Mater. Sci.*, 2006, **41**, p 561–564
13. A.M. Elwazri, P. Wanjara, and S. Yue, Effect of Prior-Austenite Grain Size and Transformation Temperature on Nodule Size of Microalloyed Hypereutectoid Steels, *Metall. Mater. Trans. A*, 2005, **36A**, p 2297–2305
14. F. Perrard, P. Donnadiou, A. Deschamps, and P. Barges, TEM Study of NbC Heterogeneous Precipitation in Ferrite, *Philos. Mag.*, 2006, **86**(27), p 4271–4284
15. R.D.K. Misra, H. Nathani, J.E. Hartmann, and F. Siciliano, Microstructural Evolution in a New 770 MPa Hot Rolled Nb-Ti Microalloyed Steel, *Mater. Sci. Eng. A*, 2005, **394**, p 339–352
16. A. Ghosh, B. Mishra, S. Das, and S. Chatterjee, Microstructure, Properties, and Age Hardening Behavior of a Thermomechanically Processed Ultralow-Carbon Cu-Bearing High-Strength Steel, *Metall. Mater. Trans. A*, 2005, **36A**, p 703–713
17. H.R. Najafi, J. Rassizadehghani, and S. Asgari, As-Cast Mechanical Properties of Vanadium/Niobium Microalloyed Steels, *Mater. Sci. Eng. A*, 2008, **486**, p 1–7
18. P. Marshal, Development of Microstructure to Optimize Mechanical Performance of power Generation Equipment, *MiCon 86: Optimization of Processing, Properties, and Service Performance Through Microstructural Control*, ASTM Special Technical Publication 979, B.L. Bramfitt, R.C. Benn, C.R. Brinkman, G.F. Vander Voort, Ed., American Society for Testing and Materials, Philadelphia, 1988, p 3–46
19. Y. Ochi, T. Matsumura, K. Masaki, and S. Yoshida, High Cycle Rotating Bending Fatigue Property in Very Long Life Regime of High-Strength Steels, *Fatigue Fract. Eng. Mater. Struct.*, 2002, **25**, p 823–830
20. K. Tanaka and Y. Akiniwa, Very High Cycle Fatigue Behavior of High Strength Steels, *Fatigue Fract. Eng. Mater. Struct.*, 2002, **25**, p 775–784